In situ cross-linking construction of 3D mesoporous bimetallic phosphide-in-carbon superstructure with atomic interface toward enhanced sodium ion storage performance

Chunrong Ma [a], Yang Hou [b], Kai Jiang [c], Long Zhao [c], Tristan Olsen [d], Yanchen Fan [e], Jiali Jiang [a], Zhixin Xu [f], ZiFeng Ma [f], Dominik Legut [e], Hui Xiong [d], Xian-Zheng Yuan [a,*]

[a] *Shandong Key Laboratory of Water Pollution Control and Resource Reuse, School of Environmental Science and Engineering, Shandong University, Qingdao, Shandong 266237, China*
[b] *Key Laboratory of Biomass Chemical Engineering of Ministry of Education, College of Chemical and Biological Engineering, Zhejiang University, Hangzhou, Zhejiang 310027, China*
[c] *State Key Laboratory of Advanced Electromagnetic Engineering and Technology, School of Electrical and Electronic Engineering, Huazhong University of Science and Technology, Wuhan, Hubei 430074, China*
[d] *Micron School of Materials Science and Engineering, Boise State University, Boise, ID 83725, USA*
[e] *IT4Innovations, VSB-Technical University of Ostrava, 17.listopadu 2172/15, CZ-70800 Ostrava, Czech Republic*
[f] *Shanghai Electrochemical Energy Devices Research Centre, School of Chemistry and Chemical Engineering, Shanghai Jiao Tong University, Shanghai, 200240, China*

ARTICLE INFO

ABSTRACT

Constructing heterostructures are capable of offering fascinating performance for electronics owing to the built-in charge transfer driving force. However, exploring a universal methodology to rationally design and controllable synthesis of heterostructure with high stability of interface is a big challenge. Also the synergistic effect of the heterointerface in the composites remains to be clarified. Here, we report three-dimensional (3D) FeP/CoP heterostructure embedded within N-doped carbon aerogel (FeP/CoP-NA) through an in situ cross-linking and phosphorization process. In such a 3D hybrid, the FeP/CoP heterocrystals are wrapped by N-doped carbon which form a core-shell structure. Benefiting from the unique porous network induced by N-doped carbon, the conducting highway is built to promote the ion and electron fast diffusion. This structure can accommodate the volume change of FeP/CoP, which prevent the agglomeration and act as the protecting layer to maintain the integrity of the interface. Impressively, the atomic interface between FeP/CoP is successfully constructed, which could not only introduce enhanced capacitive contribution to facilitate electron transport, but also provide extra active sites to adsorb more Na$^+$ proved by both experiments and density functional theory (DFT) calculations. As expected, FeP/CoP-NA electrode demonstrates an excellent rate capability of 342 mAh g^{-1} at a current of 5 A g^{-1}, a high specific capacity of 525 mAh g^{-1} at 0.2 A g^{-1}, and a long cycling stability over 8000 cycles at high current density.

1. Introduction

Lithium ion batteries (LIBs) are the current state-of-the art energy storage devices, and have been widely used in personal portables devices and electric vehicles because of their high energy storage density and long cycling life [1–3]. With the booming electrics markets and the development of large-scale energy storage devices, the rising cost caused by the limited lithium resources and uneven distribution will seriously hinder the sustainable development of LIBs [4]. In this situation, sodium ion batteries (SIBs) as desirable alternatives have returned to the spotlight due to their lower cost and abundant sodium reserves [5,6]. However, the large size of Na$^+$ (~1.02 Å) leads to the sluggish kinetics and severer volume expansion caused by more difficult Na$^+$ insertion/extraction, which results in capacity fading and poor cycle stability [7]. Therefore, the key to enhance Na$^+$ storage performance lies in exploring suitable anode materials with features of stable microstructure, fast ion diffusion, and high energy density.

Compared with insertion-type anode, conversion-type materials

---

have the advantage to achieve high energy density owing to their high specific capacity [8–12]. Nevertheless, these materials with the conversion mechanism suffer from severe volume change and poor kinetics, which limits their applications [13]. To address the above issues, the most effective solution is nanostructuring through robust carbon scaffold, which could not only shorten ion diffusion path but also effectively relieve stress during repeat Na$^+$ insertion/extraction [14,15]. Although the electrochemical performance can be enhanced to some extent, the sluggish kinetics is still a big challenge to achieve high power density SIBs. Hence, exploring an effective solution to maintain structural stability while enhancing the reaction kinetics is crucial. Recently, heterointerface constructed by bimetallic compounds with different band gaps are drawing wide attention, such as TiO$_2$/MoS$_2$ [16], SnS/SnO$_2$ [17], and MoO$_2$/TiO$_2$ [17–21]. The internal electric field at interface and abundant phase boundaries could contribute to the enhanced pseudocapacitive to promote Na$^+$ and electrons transfer, thus boosting rate capability. However, the reported bimetallic compounds mainly exhibit in the form of dentrites/dumbbell due to significant lattice mismatch, leading to poor interface compatibility and weak bonding. It is hard to realize the long-term cycling stability because the huge stress caused by the volume change which tends to result in collapse and partial aggregation [21–23]. For conversion-type anode, the rate capability and structural stability have be taken into account. Therefore, it is great urgency and challenge to explore effective way to enhance power density and cycle life for practical Na$^+$ storage.

Here, we develop the in situ formation of three-dimensional (3D) FeP/CoP heterostructure embedded in N-doped carbon aerogel (FeP/CoP-NA) by combining a cross-linking and a phosphorization process, where bimetallic FeP/CoP nanoparticles are wrapped by N-doped carbon to form the core-shell structure. The 3D porous network induced by N-doped carbon can form the conducting highway to promote the fast ion and electron diffusion, accommodate the volume change of FeP/CoP, and prevent the agglomeration and act as the protecting layer to maintain the integrity of the interface. Benefitting from the combination of the favorable features, the as-prepared FeP/CoP-NA demonstrates high rate performance (342 mAh g^{-1} at current of 5 A g^{-1}), enhanced specific capacity (525 mAh g^{-1} at 0.2 A g^{-1}) and ultralong cycling life (over 8000 cycles at current of 5 A g^{-1}). Density functional theory (DFT) and electrochemical analysis reveal that atomic interface constructed by FeP and CoP could offer a more energetically favored process for both storage capacity and diffusion kinetics, demonstrating superior synergetic effect between FeP and CoP.

2. Results and discussion

The synthesis process of FeP/CoP-NA is illustrated in Scheme 1. The alginate sol was dropped into the Fe^{3+}/Co^{2+} solution, then the aerogel particles (Figure S1) were obtained. This is mainly because alginate has ability to capture Fe^{3+}/Co^{2+} to form the "core-shell" nanostructure, then the guluronic acid chains self-assemble into the cross-linked aerogel [24]. After freeze-drying and phosphorization, the gels was transformed into the FeP/CoP-carbon hybrid. The morphology of the obtained FeP/CoP-NA is characterized by scanning electron microscopy (SEM) and transmission electron microscopy (TEM). Fig. 1a shows an interconnected and porous 3D network with continuous pores (micron diameters). As shown in the high-resolution SEM image (Fig. 1b), the ultrafine FeP/CoP nanoparticles are uniformly wrapped by the N-doped carbon assembled into the chains, and the chains fully interconnected. The TEM images (Fig. 1c and d) illustrates that all FeP/CoP nanoparticles with an average diameter of ~5 nm are encapsulated into N-doped carbon and show a typical core-shell structure. Additionally, no bare FeP/CoP nanoparticles were observed. And a uniform carbon layer of ~2 nm can be detected on the FeP/CoP nanoparticles surface, which was derived from the carbonization of biopolymer (alginate). During the carbonization process, the alginate can in-situ form a carbon layer on metal nanoparticles, which can effectively suppress the aggregation of the active particle and alleviates the stress during the charge-discharge process [25]. From the high-resolution TEM images (Fig. 1 e and f), it should be noted that several different lattice spaces are detected, which confirms the presence of different species. The lattice fringes with d = 0.25 nm can be attributed to the (2 0 0) crystal plane of CoP, whereas the lattice fringes with d = 0.27 nm corresponding to the (0 1 1) crystal plane of FeP. Interestingly, the angular mismatch and lattice boundaries between (0 1 1) plane of FeP and (2 0 0) plane of CoP can be clearly seen,
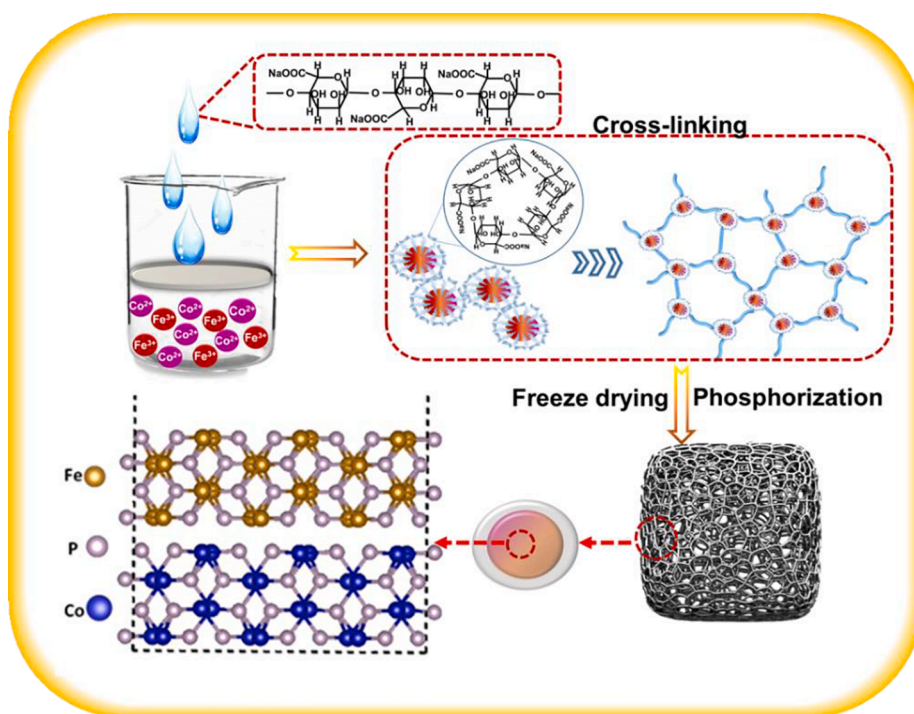
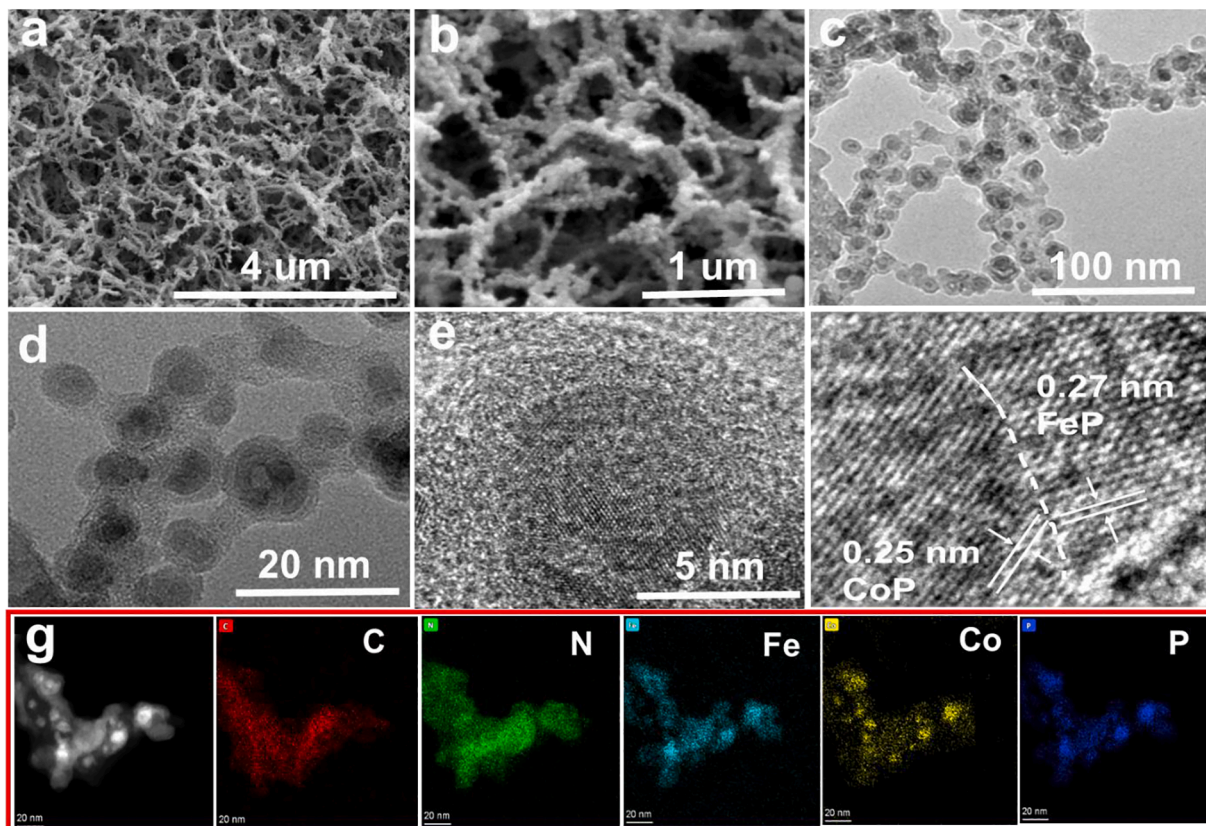**Scheme 1.** Schematic illustration of FeP/CoP-NA synthesis.

Fig. 1. (a-b) SEM images, (c-d) TEM images, (e-f) HRTEM images, and (g) Elemental mapping images of FeP/CoP-NA.

which strongly support the phase interface relationship. Such atomic interface can be expected to offer enhanced electrochemical performance for Na^+ storage. From the energy dispersive X-ray (EDX) elemental mapping results shown in Fig. 1g, elements C, N, Fe, Co, and P are homogenously distributed in the hybrids, which further confirm the existence of FeP and CoP in the composite.
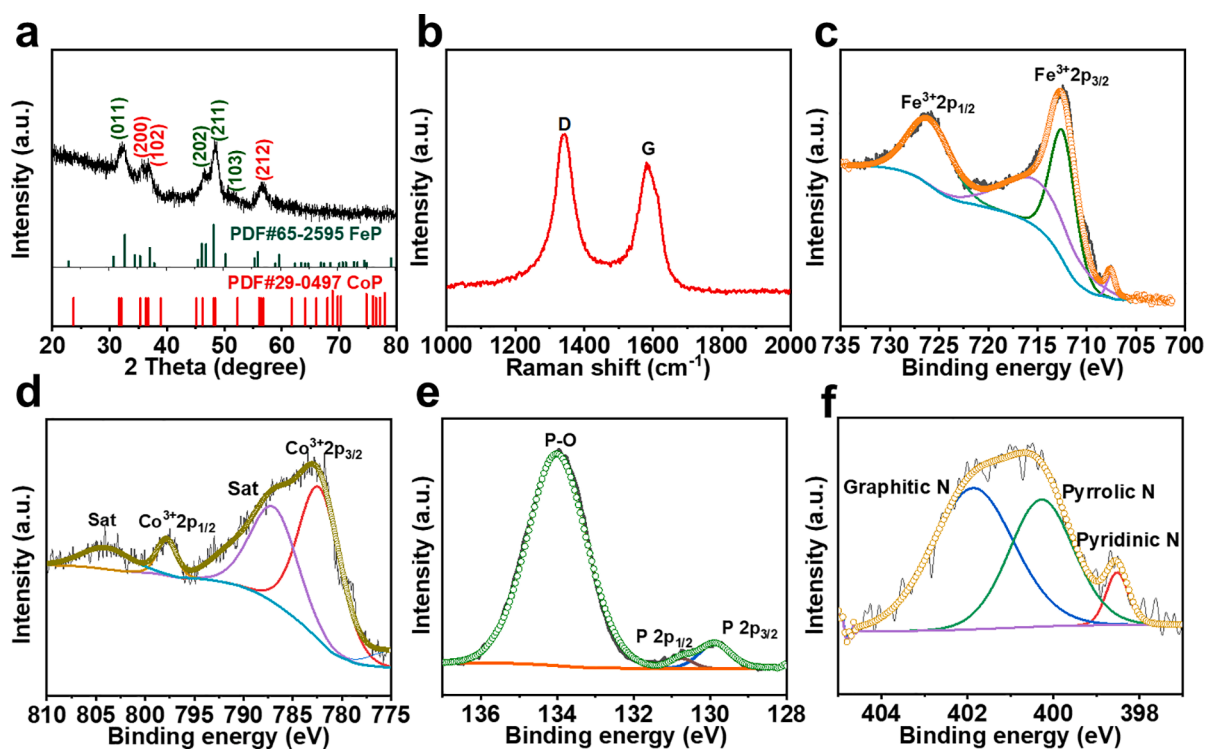

Fig. 2. (a) XRD pattern, (b) Raman spectra, (c-f) Fe 2p, Co 2p, P 2 and N 1s high-resolution XPS spectra of FeP/CoP-NA.

The crystal structure of FeP/CoP-NA was analyzed by XRD. As shown in Fig. 2a, sharp characteristic peaks can be seen, which are representative of the crystal structure of as-prepared FeP/CoP-NA. The peaks at 32.7°, 46.9°, 48.3°, 50.3° correspond to the (011), (202), (211), and (103) planes of FeP (JCPDS No: 65-2595), and the other diffraction peaks at 35.3°, 36.6°, and 56.3° are representative of the (200), (102), and (212) planes of CoP (JCPDS No: 29-0497), respectively. All the peaks can be well indexed without additional peaks, illustrating the high purity of FeP/CoP-NA. Raman spectra is shown in Fig. 2b, there are two distinct peaks at 1397 and 1587 cm^{-1}, which were assigned to the D (sp^2 C caused by defects) and G (sp^2 graphite carbon), respectively [26,27]. The relative intensity of I_D/I_G reflects the disorder degree of carbon. From the Raman results, the I_D/I_G is 1.23, suggesting an amorphous nature and more defects in the carbon induced by the N-doping, which could afford more active sites and high conductivity [28]. To further investigate the chemical state and composition of the FeP/CoP-NA, X-ray photoelectron spectroscopy (XPS) was carried out. From the XPS spectra (Figure S2a), the elements of Fe, Co, P, C and N are all present in the composite, and no other impurities were detected. In the high resolution Fe 2p XPS spectrum (Fig. 2c), two peaks with binding energy of 713.2 and 725.6 eV can be clearly observed, which correspond to the Fe $2p_{3/2}$ and Fe $2p_{1/2}$, respectively [29]. And the other peaks located at 708 eV and 716.8 eV can be ascribed to the FeP [29,30]. To further confirm the heterojunction in FeP/CoP-NA composite, the surface electronic state of Fe in mixture of FeP -NA and CoP-NA (FeP -NA and CoP-NA are physically mixed by grinding without heterojunction) is detected. Compared with the spectrum of mixture of FeP-NA and CoP-NA (Figure S3), the Fe^{3+} characteristic peaks in FeP/CoP-NA sifted to higher binding energy values, which can be attributed to the coupling effect of FeP and CoP in FeP/CoP-NA composite[17,31]. In the high resolution Co 2p XPS spectra (Fig. 2d), the two peaks located at 781.6 and 796.8 eV can be attributed to the Co $2p_{3/2}$ and Co $2p_{1/2}$, respectively, while the other peaks centered at 787.2 and 804.1 eV were related to the corresponding satellite peaks [32]. The P 2p high

resolution results are shown in Fig. 2e, the two peaks at 130.8 and 129.6 eV can be explained to the P $2p_{3/2}$ and P $2p_{1/2}$, and the other peak located at 133.8 eV correspond to the P-O which is caused by the oxidation of P under ambient air [33]. The N 1s high resolution spectrum can be deconvoluted into three peaks, in which the peaks at 402.2 eV, 400.3 eV, and 398.5 eV are ascribed to graphitic N, pyrrolic N, and pyridinic N, respectively [34] . The C1s high resolution spectrum (Figure S2b) shows three clear characteristic peaks at binding energy of 284.8, 286.2, and 288.5 eV, respectively, which can be assigned to the C–C, C–P and sp^3 C [35]. The content of FeP/CoP in FeP/CoP-NA composite is determined by thermogravimetric analysis (TGA) in air atmosphere from room temperature to 900 °C. As shown in Figure S4, the TGA curve exhibits an initial decrease within 200 °C, and then followed by a continuous weight increase. The carbon content cannot be distinguished from this process because the combustion of carbon and oxidation of CoP/FeP occurred simultaneously. As reported in literature, FeP and CoP can be transformed into $FePO_4$ and $Co_2P_2O_7$ at high temperature [36,37], respectively. According to the above analysis, the content of Fe/CoP in the composite is calculated to be ~64%.

The electrochemical performance of as-prepared FeP/CoP-NA was examined by using 2032 coin cells with sodium metal as the counter electrode. Fig. 3a shows the discharge-charge profiles of FeP/CoP-NA electrode at 1st, 10th, and 50th cycle in the voltage of 0.01–3 V at 0.2 A g^{-1}. The discharge specific capacity of 789 mAh g^{-1} and charge specific capacity of 523 mAh g^{-1} were delivered, respectively, corresponding to the initial Coulombic efficiency (CE) of 66.3%. The large irreversible specific capacity is mainly attributed to the formation of solid electrolyte interphase (SEI) film during the first cycle [38]. Notably, the discharge profile demonstrates a sloping plateau at ~1.0 V, which can be explained to the initial sodiation process and SEI film formation [38]. This sloping plateau was shifted to higher voltage (~1.2 V) in the following cycles, owing to Na^+ insertion into CoP and FeP. The CE can quickly reach ~99.5% in the 10th cycle and well maintained in the 50th cycle. Additionally, their discharge–charge profiles almost
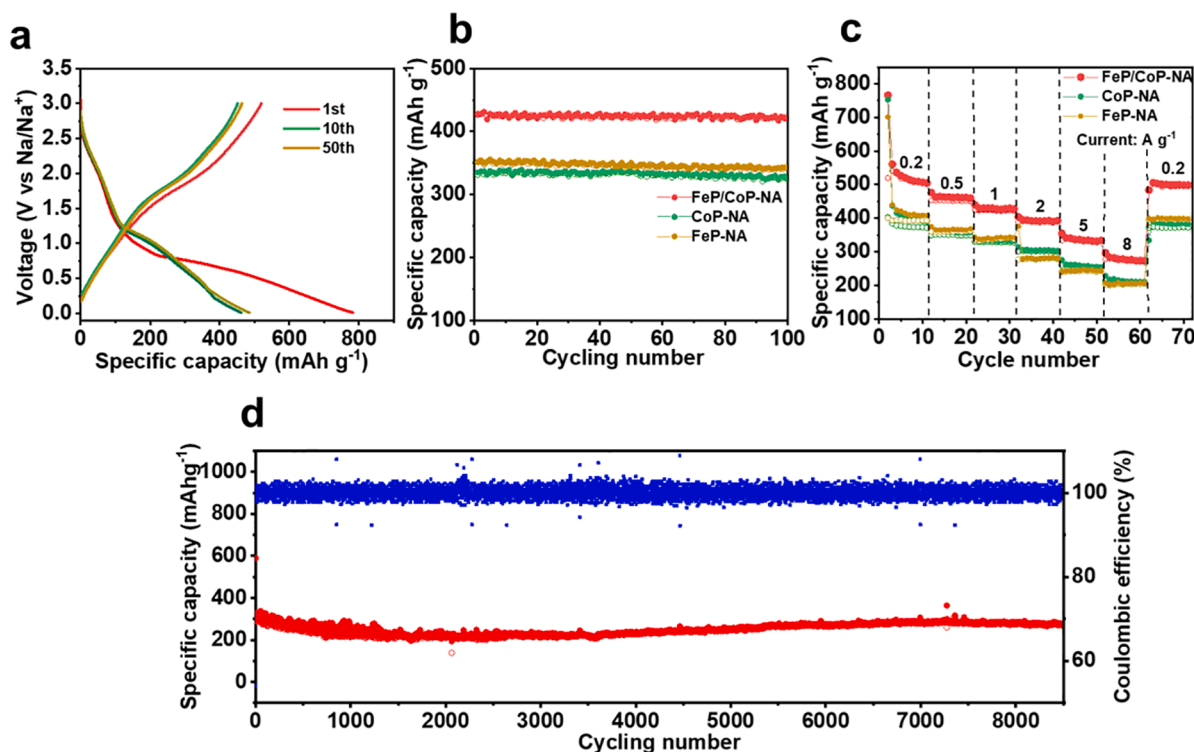

Fig. 3. (a) Charge-discharge profiles of FeP/CoP-NA at current of 0.5 A g^{-1}, (b) Cycling performance of FeP/CoP-NA, FeP–NA, and CoP-NA electrodes at current of 0.5 A g^{-1}, and (c) Long-term cycling of FeP/CoP-NA electrode at current of 5 A g^{-1}.

C. Ma et al.

overlapped, showing a high reversibility upon cycling. Fig. 3b shows the cycling performance of FeP/CoP-NA, FeP-NA, and CoP-NA electrodes at a current of 0.5 A g^{-1} between 0.01 and 3 V (after activation under the current of 0.2 A g^{-1}). The FeP/CoP-NA electrode maintains a high specific capacity of 425 mAh g^{-1} at a current of 0.2 A g^{-1} for 100 cycles without obvious degradation. For the FeP-NA, and CoP-NA electrodes, they were found to have only ~346 and 338 mAh g^{-1} specific capacity, respectively, which confirms the enhancement in capacity by engineering such atomic interfaces. The cycling performance of N-doped carbon is comparatively evaluated at the current density of 0.5 A g^{-1} with a view to investigate the effect in FeP/CoP-NA composite. As shown in Figure S5a, the electrode demonstrate gradual capacity fading in the cycling process, finally retaining only 68 mAh g^{-1} after 100 cycles. To further confirm the effect of heterojunction, the mixture of FeP–NA and CoP-NA was cycled as a control, at current of 0.5 A g^{-1}. For the mixture electrode (Figure S5b), a specific capacity of 302 mAh g^{-1} is delievered, which is lower than that of FeP/CoP-NA. The rate capability of FeP/CoP-NA was further evaluated at various current densities from 0.2 to 8 A g^{-1}. Compared to the FeP–NA and CoP-NA electrods, the FeP/CoP-NA electrode deliveres a higher specific capacity at the various current densities. The FeP/CoP-NA electrode demonstrates a high specific capacity of ~508 mAh g^{-1} at current of 0.2 A g^{-1}, which is much better than FeP–NA (403 mAh g^{-1}) and CoP-NA (391 mAh g^{-1}) electrodes. Moreover, the enhanced initial Coulombic efficiency (66%) of FeP/CoP-NA electrode is obtained (higher than that of FeP–NA (53%) and CoP-NA (51%) electrodes). With the increased current densities, the FeP/CoP-NA electrode still shows 425, 402, and 373 mAh g^{-1} specific capacity at 1, 2, and 5 A g^{-1}, respectively. At ultrahigh current density (8 A g^{-1}), a high specific capacity of 297 mAh g^{-1} is obtained, which illustrates the fast charge/discharge characteristic of FeP/CoP-NA electrode. When the current density decreased to 0.2 A g^{-1}, the corresponding specific capacity can be returned to ~500 mAh g^{-1}. The long-term cycling life is vital for the application of SIBs. However, the large Na$^+$ radius easily destroys the structural integrity caused by the huge volume change during the repeat sodiation/desodiation. The long cycling performance of FeP/CoP-NA electrode is evaluated at a high current density of 5 A g^{-1}. Impressively, the as-prepared FeP/CoP-NA electrode shows superior cycling stability without obvious capacity fluctuation during the whole process. After 8500 cycles, reversible specific capacity of 300 mAh g^{-1} can be maintained with the stable CE of ~100%, corresponding to a high capacity retention of ~92%. The morphology of the FeP/CoP-NA electrode after 50 deep charge/discharge cycles was characterized by TEM. As show in Figure S6 a, the core-shell structure is still well maintained and the FeP/CoP nanocrystal were well encapsulated in the N-doped carbon, demonstrating the high structural stability. Moreover, the atomic force microscope (AFM) was conducted to further detect the surface change of the electrode before and after cycles (Figure S6 b-c). Compared to the initial state, the electrode after 50 cycles keeps flat with slight protrusion due to Na$^+$ intercalation and extraction, which illustrates the designed 1 D core-shell structure can effectively accommodate the volume change during the charge/discharge process to ensure the high structural stability. Such results further demonstrate the highly reversible and stable nature of the atomic interface structure. The electrochemical performance of FeP/CoP-NA is compared with those reported in literatures (Figure S7), which are superior to most reported values for FeP or CoP andoes.

To reveal the structural change during the first discharge-charge process, FeP/CoP-NA electrodes at different states (as shown in Fig. 4a) were analyzed by *ex situ* XRD and TEM. From the *ex situ* XRD patterns, the characteristic peaks of Na$_3$P and Co are detected when the electrode is discharged to 0.5 V, which illustrates the metal phosphides has transformed into metal and Na$_3$P during the electrochemical reduction process. It is consistent well with the cathodic peak at ~0.6 V in the first CV curve, relating to the Na$^+$ insertion process of CoP and FeP [39]. When the FeP/CoP-NA electrode is fully discharged to 0.01 V, the primary diffraction peaks totally diminishes and more characteristic
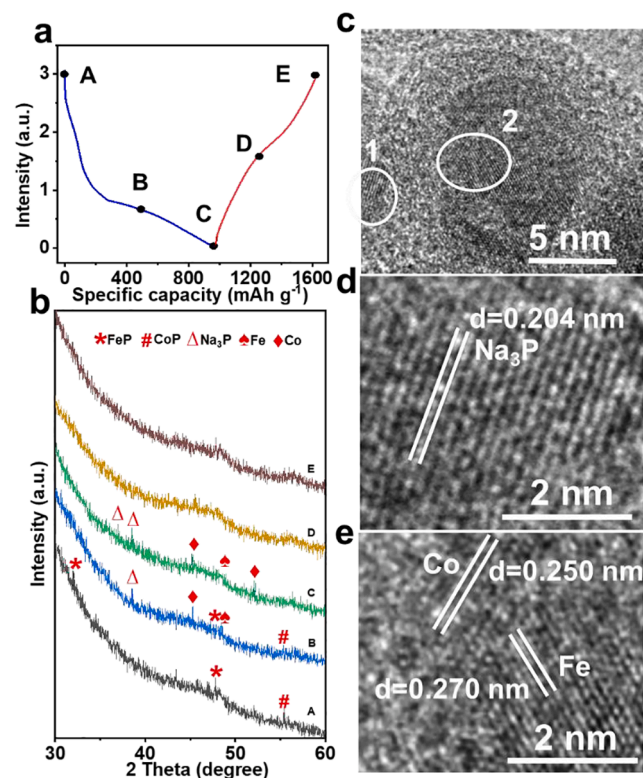

Fig. 4. (a) The discharge-charge profile of FeP/CoP-NA electrode in the first cycle, (b) The ex situ XRD pattern of FeP/CoP-NA electrode at different state dedicated on the curve, (c) TEM image of FeP/CoP-NA electrode discharged at 0.01 V, and (d) and (e) The enlarged TEM images corresponding to 1 and 2 areas of image, respectively.

peaks can be clearly observed. The peaks located at 36.0°, 37.2° are corresponding to the (110) and (103) planes of Na$_3$P (PDF 74-1164), while peaks at 49.2° and 53.0° are related to the (101) plane of Fe (PDF 34-0529) and (200) plane of Co (PDF 88-2325). The disappearance of primary FeP and CoP is accompanied by a gradual appearance of metal and Na$_3$P can be described by the following equation [40]:

$$FeP(CoP) + 3Na^+ + 3e^- \rightarrow Fe(Co) + Na_3P \tag{1}$$
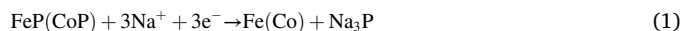
According to the above reaction process, the calculated theoretical capacity of FeP/CoP electrode is 908 mA h g^{-1}, which is close to the specific capacity of FeP/CoP electrode delivered in the first Na$^+$ insertion process (798.4 mA h g^{-1}). When the electrode switched to the charge process, no characteristic peak appear, which demonstrate the poor crystallization of charging products [41]. To further confirm the alloying mechanism of FeP/CoP-NA electrode, *ex situ* TEM was used to detect the phase change. Fig. 4c shows the TEM image of the FeP/CoP-NA electrode discharged to 0.01 V, the morphology is well-retained after Na$^+$ insertion, which illustrate the robust and stable of FeP/CoP-NA composite. Moreover, different phases can be observed from the corresponding enlarged TEM image (Fig. 4d and e). The lattice fringes with interplanar distance of 0.204 nm correspond well with the (103) plane of Na$_3$P, whereas the lattice spacing of 0.250 and 0.270 nm can be ascribed to the (111) plane of Co and the (101) plane of Fe, respectively. These results are consistent with the *ex situ* XRD pattern of the products discharged at 0.01 V, coinciding with the thoroughly electrochemical reaction according to Eq (1)

The Na$^+$ storage behavior of FeP/CoP-NA was analyzed by cyclic voltammetry (CV). The CV curves at a scan rate of 0.1 mV s^{-1} in a voltage range of 0.01–3 V are displayed in Fig. 5a. There is a clear peak at 1.1 V in the cathodic process, which can be attribute to the insertion reaction of Na$^+$ into FeP and CoP.[7] Another broad peak at ~0.7 V is
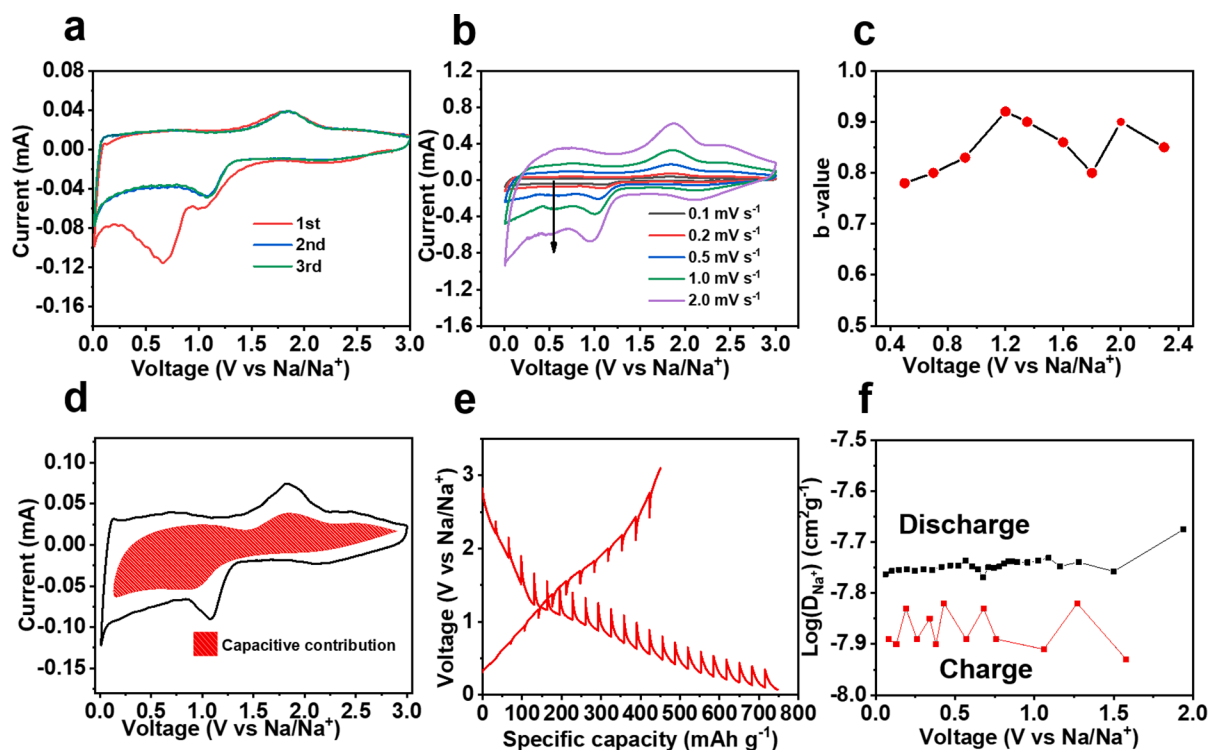
Fig. 5. (a) CV curves at scan rate of 0.1 mV s^{-1}, (b) CV curves at various scan rates from 0.1 to 2.0 mV s^{-1}, (c) A serious of b-value at corresponding voltages, (d) CV curve with capacitive contribution shaded area at scan rate of 0.2 mV s^{-1}, (e) GITT profile, and (f) Na$^+$ diffusion coefficient at different voltage of FeP/CoP-NA.

ascribed to the SEI formation [38]. During the following cycle, this peak disappeared, which demonstrates the irreversibility of this process. The main peak in the second cycle shift to a higher voltage (~1.2 V) because of the drastic structural or textural modification in the initial sodiation process, and this phenomena is common for metallic-based anode materials of SIBs [42–46]. Furthermore, both the cathodic and anodic curves overlapped well for the 2nd and 3rd cycles, illustrating the excellent electrochemical reversibility and stability of the electrode material. The CV curves at different scan rates were also analyzed to further investigate the electrochemical kinetics. Fig. 5b shows the CV curves from 0.1 to 2 mV s^{-1}, which demonstrate a similar shape. There is a power-law relationship between the current (*i*) and scan rate (*v*) [47]:

$$i = av^b \tag{2}$$

where a and b are the adjustable parameters, and the b value can be obtained by calculating slops of log(*v*)–log(*i*) plots (Figure S8). Specifically, the b values varies from 0.5 to 1, which could provide a basis for the charge storage. When b equals 1.0, the charge storage is totally controlled by capacitive behavior. A b value of 0.5 represents a diffusion-controlled process. In Fig. 5c, the b value during the cathodic process was calculated being higher than 0.8, indicating capacitive-controlled characteristics. To better distinguish the capacitive-controlled behavior in the whole charger storage at the specific scan rate, which can be quantitatively separated according to the following equation [47]:

$$i = k_1v + k_2v^{1/2} \tag{3}$$

where the k_1v represents the capacitive contribution, which can be obtained by calculating k_1. As shown in Fig. 5d, the typical voltage profile for the capacitive current (red shadow area) in comparison to the total current is plotted, and a high capacitive contribution of 85.6% is achieved for the FeP/CoP-NA at 0.2 mV s^{-1}, which contribute to the fast electrochemical kinetics. To further interpret the superior Na$^+$ storage performance of FeP/CoP-NA, galvanostatic intermittent titration

technique (GITT) technology were conducted to explore the effect of atomic interface on Na$^+$ diffusion. As shown in Fig. 5e, GITT profile was performed to explore the Na$^+$ diffusion rate (D_{Na}^+) in the charge/discharge process. A series of D_{Na}^+ (Fig. 5f) were calculated (detailed in Figure S9) at charge and discharge process, which shows minor fluctuation between $10^{-7.6} \sim 10^{-8}$ cm^{2}s^{-1}. During the charge/discharge process, the detailed D_{Na}^+ values in FeP/CoP-NA electrode were always higher than that of FeP-NA and CoP-NA (Figure S10). The distinct difference of reaction resistance during sodiation/desodiation process are explained to the transformed electrochemical reaction mechanism. Obviously, the FeP/CoP-NA electrode exhibits the lowest reaction resistance. Such desirable results are best explained by the effects of atomic phase boundaries, which can restrict the growth of crystalline domains and produce crystal defects that facilitate fast diffusion of Na$^+$. Additionally, the out-of-step reaction of two phase phosphides can contribute to relieve the stress during charge/discharge processes, thus promoting the diffusion of Na$^+$ [48].

To further elucidate the atomic interface behavior on Na$^+$ storage and provide an atomic level justification for the enhanced electrochemical performance in the heterostructure, DFT calculation was performed. The Fermi levels of FeP and CoP before contact are shown in Fig. 6a, the work functions of the FeP (0.78 eV) demonstrate a lower Fermi level than that of CoP (1.28 eV). As shown in Fig. 6b, these Fermi levels tend to shift downwards and up wards, respectively with a built-in electric field at the interface when the heterojunction is formed. The direction of the electric field induced by the heterojunction points to FeP from CoP, which induces negative charge accumulating on the FeP side and positive charge on the FeP side. Na ions tend to adsorb on the FeP side due to the electrostatic potential between FeP and CoP, which will break the charge accumulation layer at the interface. This makes Na$^+$ diffusion in the material much easier. This greatly promotes charge-transfer kinetics and result in high-rate capability. The interface model composed of FeP/CoP was rationally designed, which has been fully optimized before calculating (Fig. 6c). In order to evaluate the adsorption energies of Na in the heterointerface, the adsorption abilities of Na
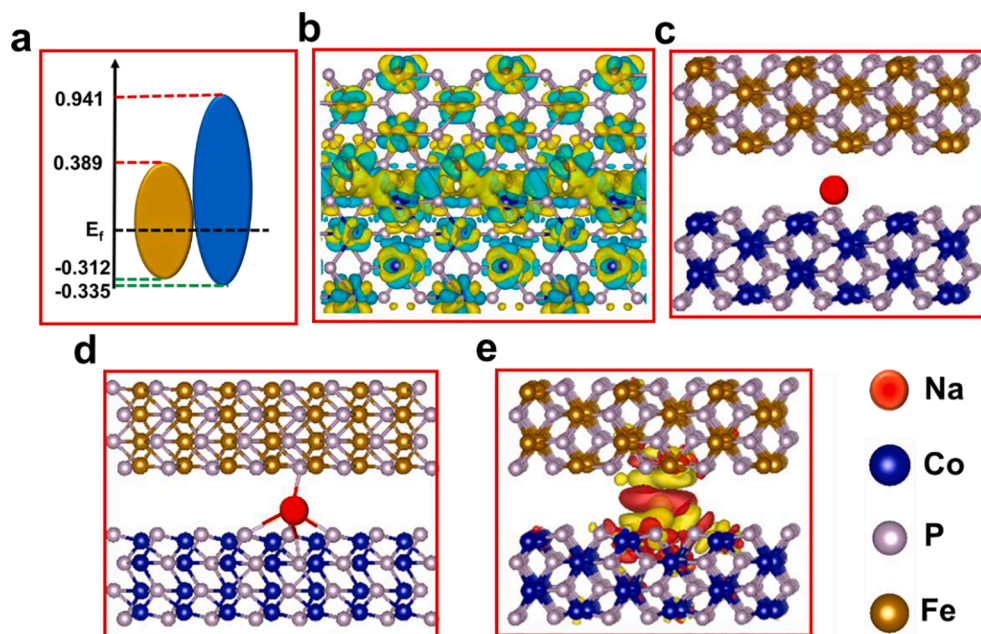
Fig. 6. DFT calculation of the electrode. (a) Calculated energy band diagram of FeP and CoP, (b) Charge density difference at interface before Na doping, (c) optimized structure of the hetero structure, (d) Na adsorption on the interface, and (e) Charge density difference in Na adsorption at interface.

on pristine FeP and CoP were also calculated (Figure S11). According to the optimizd results (Fig. 6d), the Na atom prefer to combine with four of the nearest P atoms to form Na-P bonds, while Na tend to lie on the metal site in the form of a Na-Fe or Na-Co bond. The resulting adsorption energy at heterointerface demonstrates smaller energy barriers than those at isolated FeP and CoP surface, which can be reasonably attributed to the synergetic effect from the atomic interface between FeP and CoP providing additional adsorption sites for the Na atom. The enhanced adsorption energy makes the migration of Na^+ easier during the interface compared to the pristine FeP or CoP [49]. During the sodiation process, Na atoms tend to adsorb on the superficial P atoms and act as a donor of charge transfer for the surrounding P atoms, while the metal atoms prefer to act as electron acceptors, which result in a charge separation at the interface. To better understand the charge separation, charge density difference of the interface after Na^+ sodiation was evaluated. The corresponding result is shown in Fig. 6e, the yellow and red color represent the charge accumulation and depletion, respectively. It can be seen that there is a charge redistribution associated with the sodiation process, and the Na atom is adjacent to the S layer, which result in the enhancement of binding ability [50]. Electron localization function (ELF) was further conducted to investigate the essence of the charge separation. From Figure S12, there is an average increase of 1 e in the P atom region, while the electron increase around Na atom and other atoms is 0.4. Such distribution illustrates that Na atoms interacts electrostatically with the P atoms on the heterosurface and contribute charge to P atoms, which clearly supports a charge separation on the surface, that offers extra sites for ion storage.

Based on the calculating results, the outstanding electrochemical performance can be ascribed to: (a) the 3D high conductive N-doped carbon network that not only relieves stress caused by the volume change but also increases the charge transfer efficiency, contributing to the excellent structural stability and high electrical conductivity. (b) the core-shell structure can prevent the aggregation of the active materials and act as a binder to effectively suppress the continual rupturing and reformation of the SEI. (c) the rich defective-type nitrogen in carbon shell and abundant phase boundaries of bimetallic phosphides enhances the electronic and ionic conductivity, enhancing the reversibility of reaction. (d) the unique hierarchical heterostructure with N-doped carbon promotes the enhanced pseudocapacitance behavior and demonstrates

small polarization to stimulate the restricted reaction, accelerating the kinetic reaction in charge transfer and transport. (d) the atomic interface of bimetallic phosphide provides favorable Na^+ storage sites and superior ions diffusion kinetics compared with the single metallic counterpart.

3. Conclusions

In conclusion, a 3D FeP/CoP heterostructure embedded in N-doped carbon aerogel has been developed via an effective approach. Such hierarchical core-shell structure can form the perfect atomic interface contact between bimetallic phosphides, contributing to the maximization of synergistic interaction. Notably, the unique space-confined structure can accommodate the volume expansion during charge/discharge, and prevent the aggregation of active particles. Moreover, the abundant phase boundaries promote pseudocapacitive behavior, which further boosts the electrochemical kinetics. Benefiting from the unique structure, the FeP/CoP-NA features excellent rate capability (342 mAh g^{-1} at current of 5 A g^{-1}) and outstanding cycling stability (over 8000 cycles without obvious capacity decay) at high current density as an anode for sodium ion batteries. Through in-depth analysis by DFT calculations and electrochemical tests, energy storage mechanism of as-prepared FeP/CoP-NA and the role of atomic interface have been revealed. Besides the more extra active sites for Na^+ storage, the low diffusion battier at the interfacial sites remarkably enhance the ion diffusion and reaction kinetics, which is responsible for the extraordinary performance of FeP/CoP-NA electrode. Given the novel insights on interface engineering, this work will open up a prospect for the rational design of high-performance conversion reaction-based anode materials for energy storage devices.

Declaration of Competing Interest

The authors declare that they have no known competing financial interests or personal relationships that could have appeared to influence the work reported in this paper.

Acknowledgment

Appendix A. Supplementary data

Content of Supporting Information: Methods, Photography of alginate hydrogel, XPS spectra of FeP/CoP-NA, b-value, GITT technique, GITT profiles, Na+ diffusion coefficient of FeP-NA, Na adsorption on various systems optimized via DFT calculation and ELF plot at the interface before (a) and after Na doping (b).

Supplementary data to this article can be found online at https://doi.org/10.1016/j.cej.2020.127449.

References

[1] J. Bai, B. Xi, H. Mao, Y. Lin, X. Ma, J. Feng, S. Xiong, One-Step Construction of N, P-Codoped Porous Carbon Sheets/CoP Hybrids with Enhanced Lithium and Potassium Storage, Adv. Mater. 30 (2018) 1802310.

[2] G.D. Park, S.J. Yang, J.-H. Lee, Y.C. Kang, Investigation of Binary Metal (Ni, Co) Selenite as Li-Ion Battery Anode Materials and Their Conversion Reaction Mechanism with Li Ions, Small 10 (2019) 1905289.

[3] G. Jeong, Y.-U. Kim, H. Kim, Y.-J. Kim, H.-J. Sohn, Prospective materials and applications for Li secondary batteries, Energy Environ. Sci. 4 (2011) 1986–2002.

[4] C. Ma, T. Xu, Y. Wang, Advanced carbon nanostructures for future high performance sodium metal anodes, Energy Storage Mater. 32 (2020) 1806304.

[5] T. Jin, Q. Han, L. Jiao, Binder-Free Electrodes for Advanced Sodium-Ion Batteries, Adv. Mater. 32 (3) (2020), https://doi.org/10.1002/adma.201806304.

[6] J. Chen, L. Wei, A. Mahmood, Z. Pei, Z. Zhou, X. Chen, Y. Chen, Prussian blue, its analogues and their derived materials for electrochemical energy storage and conversion, Energy Storage Mater. 25 (2020) 585–612.

[7] D. Zhao, R. Zhao, S. Dong, X. Miao, Z. Zhang, C. Wang, L. Yin, Alkali-induced 3D crinkled porous Ti3C2 MXene architectures coupled with NiCoP bimetallic phosphide nanoparticles as anodes for high-performance sodium-ion batteries, Energy Environ. Sci. 12 (2019) 2422–2432.

[8] C. Ma, Z. Fu, C. Deng, X. Liao, Y. He, Z. Ma, H. Xiong, Carbon-coated FeP nanoparticles anchored on carbon nanotube networks as an anode for long-life sodium-ion storage, Chem. Commun. 54 (2018) 11348–11351.

[9] K. Zhang, Z. Zhu, J. Lin, R. Zhang, C. Zhao, One-step simultaneously heteroatom doping and phosphating to construct 3D FeP/C nanocomposite for lithium storage, Appl. Surface Sci. Appl. Surface Sci. 500 (2020), 144055.

[10] Y. Wang, Y.V. Lim, S. Huang, M. Ding, D. Kong, Y. Pei, T. Xu, Y. Shi, X. Li, H. Y. Yang, Enhanced Sodium Storage Kinetics by Volume Regulation and Surface Engineering via Rationally Designed Hierarchical Porous FeP@C/RGO, Nanoscale 10 (2020) 34–68.

[11] S. Shi, C. Sun, X. Yin, L. Shen, Q. Shi, K. Zhao, Y. Zhao, J. Zhang, FeP Quantum Dots Confined in Carbon-Nanotube-Grafted P-Doped Carbon Octahedra for High-Rate Sodium Storage and Full-Cell Applications, Adv. Funct. Mater. 10 (2020) 1909283.

[12] J. Gao, Y. Li, B. Peng, G. Wang, G. Zhang, The General Construction of Asymmetric Bowl-Like Hollow Nanostructures by Grafting Carbon-Sheathed Ultrasmall Iron-Based Compounds Onto Carbon Surfaces for Use as Superior Anodes for Sodium-Ion Hybrid Capacitors, J. Mater. Chem. A 7 (2019) 24199–24204.

[13] X. Ren, Z. Ren, Q. Li, W. Wen, X. Li, Y. Chen, L. Xie, L. Zhang, D. Zhu, B. Gao, P. K. Chu, K. Huo, Tailored Plum Pudding-Like Co2P/Sn Encapsulated with Carbon Nanobox Shell as Superior Anode Materials for High-Performance Sodium-Ion Capacitors, Adv. Energy Mater. 9 (2019) 1900091.

[14] J. Liu, P. Kopold, W. Chao, P.A.V. Aken, J. Maier, Y. Yan, Uniform Yolk-Shell Sn4P3@C Nanospheres as High-Capacity and Cycle-Stable Anode Materials for Sodium-Ion Batteries, Energy Environ Sci 8 (2015) 3531–3538.

[15] J. Hassoun, S. Panero, P. Simon, P.L. Taberna, B. Scrosati, High-Rate, Long-Life Ni–Sn Nanostructured Electrodes for Lithium-Ion Batteries, Adv. Mater. 38 (2010) 10002584.

[16] P. Qiang, Y. Zhao, X. Bian, Y. Ju, C. Gang, Hybrid Graphene@MoS2@TiO2 Microspheres for Use as a High Performance Negative Electrode Material for Lithium Ion Batteries, J. Mater. Chem. A 5 (2017) 3667–3674.

[17] Y. Zheng, T. Zhou, C. Zhang, J. Mao, H. Liu, Z. Guo, Boosted Charge Transfer in SnS/SnO2 Heterostructures: Toward High Rate Capability for Sodium-Ion Batteries, Angewandte Chemie-International Edition 55 (2016) 3408–3413.

[18] C. Ma, X. Li, C. Deng, Y.-Y. Hu, S. Lee, X.-Z. Liao, Y.-S. He, Z.-F. Ma, H. Xiong, Coaxial Carbon Nanotube Supported TiO2@MoO2@Carbon Core-Shell Anode for Ultrafast and High-Capacity Sodium Ion Storage (vol 13, pg 671, ACS Nano 13 (2019) (2019) 2664.

[19] Y.-Q. Wu, H.-X. Yang, Y. Yang, H. Pu, W.-J. Meng, R.-Z. Gao, D.-L. Zhao, SnS2/Co3S4 Hollow Nanocubes Anchored on S-Doped Graphene for Ultrafast and Stable Na-Ion Storage, Small 15 (2019), 1903873.

[20] X.-M. Lin, J.-H. Chen, J.-J. Fan, Y. Ma, P. Radjenovic, Q.-C. Xu, L. Huang, S. Passerini, Z.-Q. Tian, J.-F. Li, Synthesis and Operando Sodiation Mechanistic Study of Nitrogen-Doped Porous Carbon Coated Bimetallic Sulfide Hollow Nanocubes as Advanced Sodium Ion Battery Anode, Adv. Energy Mater. 9 (2019), 1902312.

[21] H. Zhou, Z. Li, K. Wang, M. Gao, S. Ding, Phase Boundary- Enhanced Ni3N-Co3N@CNT Composite Materials for Lithium- Ion Batteries, J. Mater. Chem. A 7 (2019) 1779–1784.

[22] Y. Li, H. Wang, L. Wang, R. Wang, B. He, Y. Gong, X. Hu, Ultrafast Na+-storage in TiO2-coated MoS2@N-doped Carbon for High-energy Sodium-ion Hybrid Capacitors, Energy Storage Mater. 23 (2019) 95–104.

[23] S. Wang, F. Cao, Y. Li, Z. Zhang, D. Zhou, Y. Yang, Z. Tang, MoS2-Coupled Carbon Nanosheets Encapsulated on Sodium Titanate Nanowires as Super-Durable Anode Material for Sodium-Ion Batteries, Adv. Sci. 6 (2019), 1900028.

[24] D. Kang, Q. Liu, M. Chen, J. Gu, D. Zhang, Spontaneous Cross-linking for Fabrication of Nanohybrids Embedded with Size-Controllable Particles, ACS Nano 10 (2016) 889–898.

[25] N. Wang, Q. Liu, D. Kang, J. Gu, W. Zhang, D. Zhang, Facile Self-Cross-Linking Synthesis of 3D Nanoporous Co3O4/Carbon Hybrid Electrode Materials for Supercapacitors, ACS Appl. Mater. Interfaces 8 (2016) 16035–16044.

[26] C. Ma, H. Yang, Z. Xu, Z. Fu, Y. Xie, H. Zhang, M. Hong, Z. Ma, H. Xiong, X.-Z. Yuan, Insights Into High Capacity and Ultrastable Carbonaceous Anodes for Potassium-Ion Storage via A Hierarchical Heterostructure, J. Mater. Chem. A 8 (2020) 2836–2842.

[27] A.C. Ferrari, J. Robertson, Interpretation of Raman Spectra of Disordered and Amorphous Carbon, Physical Review B 61 (2000) 14095–14107.

[28] X. Chang, X. Zhou, X. Ou, C.-S. Lee, J. Zhou, Y. Tang, Ultrahigh Nitrogen Doping of Carbon Nanosheets for High Capacity and Long Cycling Potassium Ion Storage, Adv. Energy Mater. 10 (2019), 1902672.

[29] Y. Wang, C. Wu, Z. Wu, G. Cui, F. Xie, X. Guo, X. Sun, FeP Nanorod Arrays on Carbon Cloth: A High-Performance Anode for Sodium-Ion Batteries, Chem. Commun. 64 (2018) 9341–9344.

[30] Y. Yan, B. Zhao, S.C. Yi, X. Wang, Assembling Pore-Rich FeP Nanorods on the CNT Backbone as An Advanced Electrocatalyst for Oxygen Evolution, J. Mater. Chem. A 33 (2016) 13005–13010.

[31] E. Xu, Y. Zhang, H. Wang, Z. Zhu, J. Quan, Y. Chang, P. Li, D. Yu, Y. Jiang, Ultrafast Kinetics Net Electrode Assembled via MoSe2/Mxene Heterojunction for High-Performance Sodium-Ion Batteries, Chem. Eng. J. 385 (2020), 123839.

[32] Y. Li, J. Fang, J. Zhang, J. Yang, R. Yuan, J. Chang, M. Zheng, Q. Dong, A Honeycomb-like Co@N-C Composite for Ultrahigh Sulfur Loading Li-S Batteries, ACS Nano 11 (2017) 11417–11424.

[33] X. Wang, Z. Na, D. Yin, C. Wang, Y. Wu, G. Huang, L. Wang, Phytic Acid-Assisted Formation of Hierarchical Porous CoP/C Nanoboxes for Enhanced Lithium Storage and Hydrogen Generation, ACS Nano 12 (2018) 12238–12246.

[34] K. Share, A.P. Cohn, R. Carter, B. Rogers, C.L. Pint, Role of Nitrogen-Doped Graphene for Improved High-Capacity Potassium Ion Battery Anodes, ACS Nano 10 (2016) 9738–9744.

[35] X. Gao, J. Feng, D. Su, Y. Ma, G. Wang, H. Ma, J. Zhang, In-situ exfoliation of porous carbon nitride nanosheets for enhanced hydrogen evolution, Nano Energy 59 (2019) 598–609.

[36] J. Zhang, K. Zhang, J. Yang, G.-H. Lee, J. Shin, V. Wing-hei Lau, Y.-M. Kang, Bifunctional Conducting Polymer Coated CoP Core-Shell Nanowires on Carbon Paper as a Free-Standing Anode for Sodium Ion Batteries, Adv. Energy Mater. 8 (2018), 1800283.

[37] Y. Von Lim, S. Huang, Y. Zhang, D. Kong, Y. Wang, L. Guo, J. Zhang, Y. Shi, T. P. Chen, L.K. Ang, Bifunctional Porous Iron Phosphide/Carbon Nanostructure Enabled High-Performance Sodium-Ion Battery and Hydrogen Evolution Reaction, Energy Storage Mater. 21 (2018) 98–107.

[38] Z. Li, L. Zhang, X. Ge, C. Li, S. Dong, C. Wang, L. Yin, Core-shell Sructured CoP/FeP Porous Microcubes Interconnected by Reduced Graphene Oxide as High Performance Anodes for Sodium Ion Batteries, Nano Energy 32 (2017) 494–502.

[39] Z. Liu, Y. Sungjin, S. Bingxue, C. Xinghua, Z. Jie, L. Xingguo, Peapod-Like CoP@C Nanostructure from Phosphorization in Low-Temperature Molten Salt for High-Performance Lithium Ion Batteries, Angew. Chem. Int. Ed. 59 (2019) 1975.

[40] W.J. Li, S.L. Chou, J.Z. Wang, H.K. Liu, S.X. Dou, A New, Cheap, And Productive Fep Anode Material for Sodium-Ion Batteries, Chem. Commun. 51 (2015), 4720 4720.

[41] Z.Q. Li, L.Y. Zhang, X.L. Ge, C.X. Li, S.H. Dong, C.X. Wang, L.W. Yin, Core-shell Structured CoP/FeP Porous Microcubes Interconnected by Reduced Graphene Oxide as High Performance Anodes for Sodium Ion Batteries, Nano Energy 32 (2017) 494–502.

[42] Z. Li, L. Yin, Sandwich-Like Reduced Graphene Oxide Wrapped MOF-Derived ZnCo2O4-ZnO-C On Nickel Foam As Anodes For High Performance Lithium Ion Batteries, J. Mater. Chem. A 3 (2015) 21569–21577.

[43] Z. Bai, Z. Ju, C. Guo, Y. Qian, B. Tang, S. Xiong, Direct large-scale synthesis of 3D hierarchical mesoporous NiO microspheres as high-performance anode materials for lithium ion batteries, Nanoscale 6 (2014) 3268–3273.

[44] H. Tabassum, C. Zhi, T. Hussain, T. Qiu, R. Zou, Encapsulating Trogtalite CoSe2 Nanobuds into BCN Nanotubes as High Storage Capacity Sodium Ion Battery Anodes, Adv. Energy Mater. 10 (2019), 1901778.

[45] Q. Tan, W. Zhao, K. Han, P. Li, W. Wang, D. He, Z. Liu, Q. Yu, M. Qin, X. Qu, The multi-yolk/shell structure of FeP@foam-like graphenic scaffolds: strong P-C bonds

and electrolyte- and binder-optimization boost potassium storage, J. Mater. Chem. A 7 (2019) 15673–15682.

[46] L. David, R. Bhandavat, G. Singh, MoS_2/graphene Composite Paper For Sodium-Ion Battery Electrodes, ACS Nano 8 (2014) 1759–1770.

[47] J. Wang, J. Polleux, J. Lim, B. Dunn, Pseudocapacitive Contributions to Electrochemical Energy Storage in TiO_2 (anatase) Nanoparticles, J. Phys. Chem. C 111 (2007) 14925–14931.

[48] J. Qin, H.M.K. Sari, X. Wang, H. Yang, J. Zhang, X. Li, Controlled Design of Metal Oxide-Based (Mn^{2+}/Nb^{5+}) Anodes for Superior Sodium-Ion Hybrid Supercapacitors: Synergistic Mechanisms of Hybrid Ion Storage, Nano Energy 71 (2020) 104594.

[49] X. Lei, K. Yu, R. Qi, Z. Zhu, Fabrication and Theoretical Investigation Of MoS_2-Co_3S_4 Hybrid Hollow Structure as Electrode Material for Lithium-Ion Batteries and Supercapacitors, Chem. Eng. J. 347 (2018) 607–617.

[50] X. Li, W. Zhang, J. Cai, H. Yan, M. Cui, G. Wu, M. Li, Hierarchical Nanosheets Constructed by Integration of Bimetallic Sulfides Into N-Doped Carbon: Enhanced Diffusion Kinetics and Cycling Stability for Sodium Storage, Nano Energy 62 (2019) 239–249.